Supporting Information

Ptychographic X-ray Tomography Reveals Additive Zoning in Nanocomposite Single Crystals

Johannes Ihli, Mark A. Levenstein, Yi-Yeoun Kim, Klaus Wakonig, Yin Ning, Aikaterini Tatani, Alexander N. Kulak, David C. Green, Mirko Holler, Steven P. Armes and Fiona C. Meldrum

1. Materials

Methacrylic acid (MAA), benzyl methacrylate (BzMA), and 4,4'-azobis(4-cyanovaleric acid) (ACVA; 99%) were purchased from Sigma-Aldrich (UK). 4-Cyano-4-(2-phenylethanesulfanylthiocarbonyl)sulfanylpentanoic acid (PETTC) was prepared according to the protocol reported by Semsarilar et al.[1]. The methanolic silica sol (MA-ST) used to prepare the silica-loaded vesicles was kindly donated by Nissan Chemicals (Japan). The silica concentration in the MA-ST was determined to be 34.7% w/w using an Ohaus MB45 moisture analyzer. Ammonium carbonate and calcium chloride dihydrate were purchased from Sigma Aldrich, and were used as received. Solutions were prepared using Milli-Q water (18.2 MΩcm).

2. Synthesis and Characterisation of Diblock Copolymer Worms and Vesicles

The diblock copolymer nano-objects were synthesised as described previously using polymerization-induced self-assembly (PISA).[2, 3] Briefly, a poly(methacrylic acid) (PMAA) precursor was used for the reversible addition-fragmentation chain transfer (RAFT) dispersion polymerisation of benzyl methacrylate (BzMA) in alcoholic media. The PBzMA block forms the non-solvated worm cores and vesicle membranes, while the PMAA block acts as a steric stabiliser. The PMAA stabiliser block becomes ionised on transferring the nano-objects from alcoholic media to water via dialysis, leading to highly anionic surface character at ≈ pH 9.

Calcium carbonate is precipitated at pH 9.0 – 9.5.[2, 3] Silica nanoparticles of 12 ± 2 nm diameter were incorporated within the vesicles during their PISA synthesis, and non-encapsulated particles were subsequently removed via seven centrifugation/redispersion cycles. The first five cycles were conducted using a 73:23 ethanol/methanol mixture, and the final two cycles using deionized water. ^{1}H NMR spectroscopy analysis yielded mean diblock compositions of $PMAA_{71}$-$PBzMA_{150}$ for the worms and $PMAA_{69}$-$PBzMA_{200}$ for the vesicles.

Dynamic light scattering was used to determine the vesicle size distribution. Measurements were carried out using a Malvern Instruments Zetasizer Nano ZS instrument. Specimens were analysed in the presence of background salt (10^{-3} M KCl). The mean worm width was estimated from electron micrographs. Measurements were conducted using a FEGTEM operating at 200 kV.

3. Synthesis of Calcite Nanocomposites

Single crystals of calcite occluding either worms or vesicles were prepared using the ammonia diffusion method.[3] The worm/calcite crystals were prepared using [$CaCl_2$] = 1.25 mM and 0.01 wt% $PMAA_{71}$-$PBzMA_{150}$, while [$CaCl_2$] = 1.5 mM and 0.1 wt% $PMAA_{69}$-$PBzMA_{200}$ was used for the vesicle/calcite crystals. The reaction was allowed to proceed for 12 h in both cases. After this time the glass slides supporting the crystals were rinsed with water and ethanol, and finally dried in air.

4. Characterization of the Nanocomposite Crystals

Crystal polymorphs were determined using Raman microscopy (Renishaw 2000 inVia-Raman microscope equipped with a 785 nm diode laser). The sample composition was determined

by TGA using a TA Instruments STD Q600 at a heating rate of 10 °C min^{-1} under a 100 ml min^{-1} N_2 or air flow. Optical micrographs were acquired using a Leica M165FC stereo microscope. Scanning electron microscopy (SEM) studies of the nanocomposite crystals was carried out using an FEI Nova NanoSEM 650 instrument. Glass slides supporting the crystals were mounted on SEM stubs using adhesive pads and were coated with 2 nm of iridium.

4.1. Ptychographic X-ray Computed Tomography (PXCT)

Ptychographic X-ray computed tomography[4] is a lensless imaging technique in which the phase problem is solved by means of iterative phase retrieval algorithms. By solving the phase problem at different projection angles, ptychographic tomography retrieves the complex-valued transmissivity of the specimen, providing tomograms of both phase and amplitude contrast.[5, 6] Here and in the main text we focus on the acquired phase/ or refractive index decrement tomograms due to their superior spatial resolution.

4.2 Sample Mounting for PXCT

Single nanocomposite crystals for PXCT experiments were transferred directly from glass substrates onto oxygen-free copper (OFHC) OMNY tomography sample holder pins (tip version).[7] OMNY pins were mounted on a micromanipulator (Injectman, Eppendorf) and dipped into a UV-curable epoxy resin (NOA-81, Norland Products), where excess adhesive can be removed with a lint-free wipe. The pins were slowly lowered onto the substrate with the micromanipulator until one crystal was wetted by the epoxy and lifted off the glass by adhesion forces. The pins were then removed from the manipulator and immediately placed under a UV lamp (2.8 mW cm^{-2}, 254 nm) for 5 min to fix the crystal in place. This must be performed quickly to prevent the crystal from becoming completely embedded within the

epoxy matrix. Samples were subsequently inspected with an optical microscope after curing to ensure that the crystal was mounted at the end of the tip (Figure S3).

4.3. Data Acquisition, Tomographic Reconstruction and Spatial Resolution Estimation

PXCT experiments were carried out at the cSAXS beamline of the Swiss light source (SLS). The photon energy was set to 6.2 keV, which corresponds to an X-ray wavelength of 2 Å, using a double-crystal Si(111) monochromator. Horizontal slits located at 12 m downstream of the source, that is 22 m upstream of the sample were closed to 20 µm. This was chosen to create a horizontal virtual source point coherently illuminating a Fresnel zone plate, the latter being 220 µm in diameter with an outermost zone width of 60 nm.[8] The sample was placed 1.2 mm downstream of the zone plate's focal point, resulting in an illumination probe of ≈ 4 µm in diameter at the sample plane. For the worm/calcite nanocomposite, we acquired coherent diffraction patterns using a PILATUS 2M detector[9] with a 172 µm pixel size placed ≈ 7.34 m downstream of the sample. For the vesicle/calcite nanocomposite, we acquired coherent diffraction patterns with a 500k Eiger detector with a 75 µm pixel size placed ≈ 7.284 m downstream of the sample.[10] An evacuated flight tube was positioned between the sample and detector to reduce air scattering and absorption. Measurements were carried out using an in-vacuum version of the positioning instrumentation reported by Holler *et al*.[11, 12] at a temperature of -180°C in vacuum. Sampling positions were set using a Fermat spiral scanning grid[13] with an average step size of 1.2 µm or 2 µm, respectively.

Tomography projections were acquired using a binary acquisition strategy as described by Kaestner *et al.* with two nests of projections.[14] Approximately 1000 projections of equal angular spacing were acquired across 180°. Across samples projections were obtained by

ptychographic scans consisting of around 200 and 500 diffraction patterns, each with an exposure time of 0.1 second. The field of view covered in a projection across samples was at maximum ≈ 30 × 65 μm^2 (horizontal × vertical). To compensate for the loss of information between individual detector modules, the detector was moved perpendicular to the X-ray propagation direction by a distance slightly larger than the vertical and horizontal module gap widths after two successive projections.[11, 15] The ptychographic scan in each tomographic angle was performed only once. The detector position was alternated every two successive scans. The X-ray dose imparted to the specimens was on the order of $\approx 10^7$ Gy.[16]

From each diffraction pattern, which was acquired with the Pilatus detector, a region of 512 × 512 pixels was used in the reconstructions. The resulting pixel size is $(16.66\ nm)^3$ in the reconstructed projections. Reconstructions were obtained with 400 iterations of the difference map algorithm[5] followed by 400 iterations of maximum likelihood refinement.[17, 18] From each diffraction pattern acquired with the Eiger detector, a region of 500 × 500 pixels was used in the reconstructions. The resulting pixel size is $(38.82\ nm)^3$ in the reconstructed projections. Reconstructions were obtained with 500 iterations of the difference map algorithm[5] followed by 300 iterations of maximum likelihood refinement.[17, 18] Reconstructions were performed by sharing information on the illumination between consecutive scans taken at different projection angles[15] in order to sufficiently constrain the intensities not measured due to gaps between detector modules.[11] Prior to tomography reconstructions, the complex-valued projections were aligned and processed as described in Guizar-Sicairos *et al.*[19]. Horizontal alignment was ensured based on tomographic consistency.[20] Tomographic reconstruction of phase projections was performed using a modified filtered back-projection (FBP) algorithm.[19] To mitigate noise in the reconstruction, a Hanning filter was used. The

resulting tomograms provide the 3D distribution of the refractive index decrement, δ(**r**), and electron density away from absorption edges.[4, 21]

The half-period spatial resolution of ptychographic tomograms was estimated by Fourier shell correlation (FSC).[22] The full dataset of angular projections used for the tomographic reconstructions was divided in half, and two independent tomograms with double angular spacing were reconstructed independently. Then, the correlation between these two tomograms in Fourier domain was calculated and the resolution estimated based on the intersection with a set threshold. The threshold criteria for the FSC was the ½ bit criteria.[22] The spatial resolution of the silica-loaded vesicle/calcite nanocomposite crystal tomogram was estimated to be 56 nm. The spatial resolution of the worm/calcite nanocomposite crystal tomogram was estimated to be 65 nm. FSC line plots are shown in Figure S4.

Measurements where conducted under cryogenic conditions to mitigate any potential radiation damage of the dispersed phase, e.g. breaking of the vesicle structure.

4.4 Tomogram Analysis

Refractive index decrement tomograms were first converted to electron density as reported by Diaz et al.[21] A binary mask of the entire composites was defined by means of threshold segmentation and succeeding morphological operations. Component matching was achieved by comparing calculated electron densities of known sample components (air 0.0003 eA^{-3}, calcite 0.82 eA^{-3}, copolymer worms 0.39 eA^{-3}, silica 0.63 eA^{-3} and silica-loaded copolymer vesicle (0.36 eA^{-3}) with measured electron densities where feasible.[1, 23, 24] A comparison of

the retrieved electron densities of air with the tabulated density of air reveals a spread of less than 5% on a single-voxel level.

The individual components of the nanocomposites were isolated using threshold segmentation where feasible. Thresholds were placed midway between the calculated electron densities of the selected components. In the case of unresolved features, i.e. partial volume effects, this results in a classification of voxels dominated by a given component on a volumetric basis. Neighbourhood-based component labelling was used to identify individual occlusions, and subsequent label analysis provided size and shape distributions. Inter-composite distances between the segmented dispersed phases were calculated using Euclidean distance maps. All segmentation and morphological analysis was performed using the Avizo software package (FEI Company).

The radial distributions shown in Figures 2 and 3 are based on a three-dimensional distance map to the particle exterior, and were calculated on the basis of the above-defined binary mask. Axial distributions, e.g. in direction of a crystallographic axis, shown in Figure 4, are a result of 2D sub-volume averaged distance maps. For simplicity, electron density values were transformed first to vol.% occlusion using the theoretical electron densities of the reference components as upper and lower bounds, and then into wt.% occlusion values using mass density values where available. A density of 1.1 g cm^{-3} was used for the vesicle tomogram, and 1.24 g cm^{-3} for the worm tomogram.

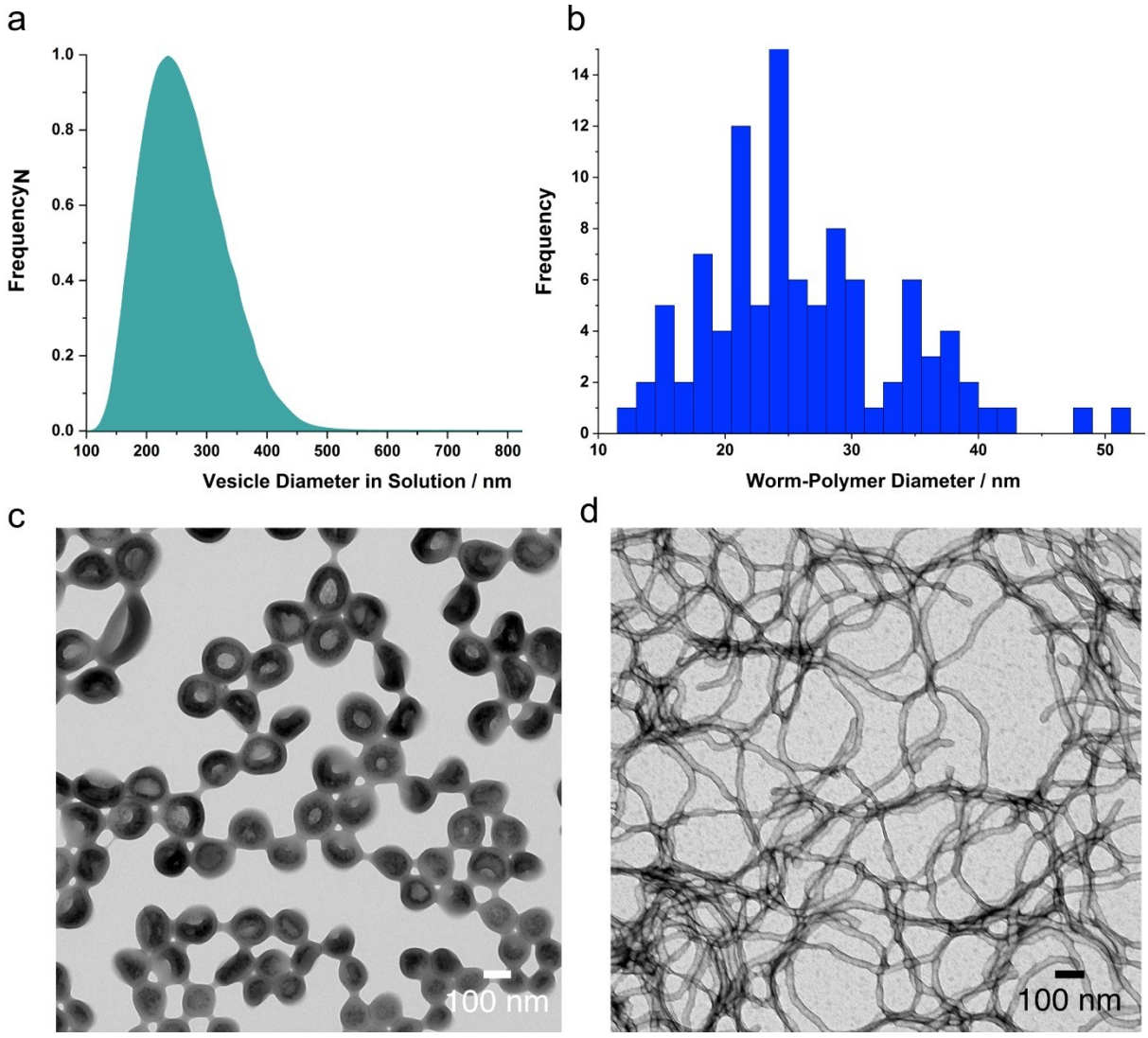

Figure S1: Diblock Colymer Nano-Object Size Prior to Occlusion. (a) Dynamic light scattering was used to determine the particle size distribution of the $PMAA_{69}$-$PBzMA_{200}$ vesicles in solution.[2] (b) The mean width of the $PMAA_{71}$-$PBzMA_{150}$ worms is estimated from electron micrographs.[3] (c and d) TEM images of (c) $PMAA_{71}$-$PBzMA_{150}$ worms and (d) $PMAA_{69}$-$PBzMA_{200}$ vesicles dried onto a TEM grid and stained.

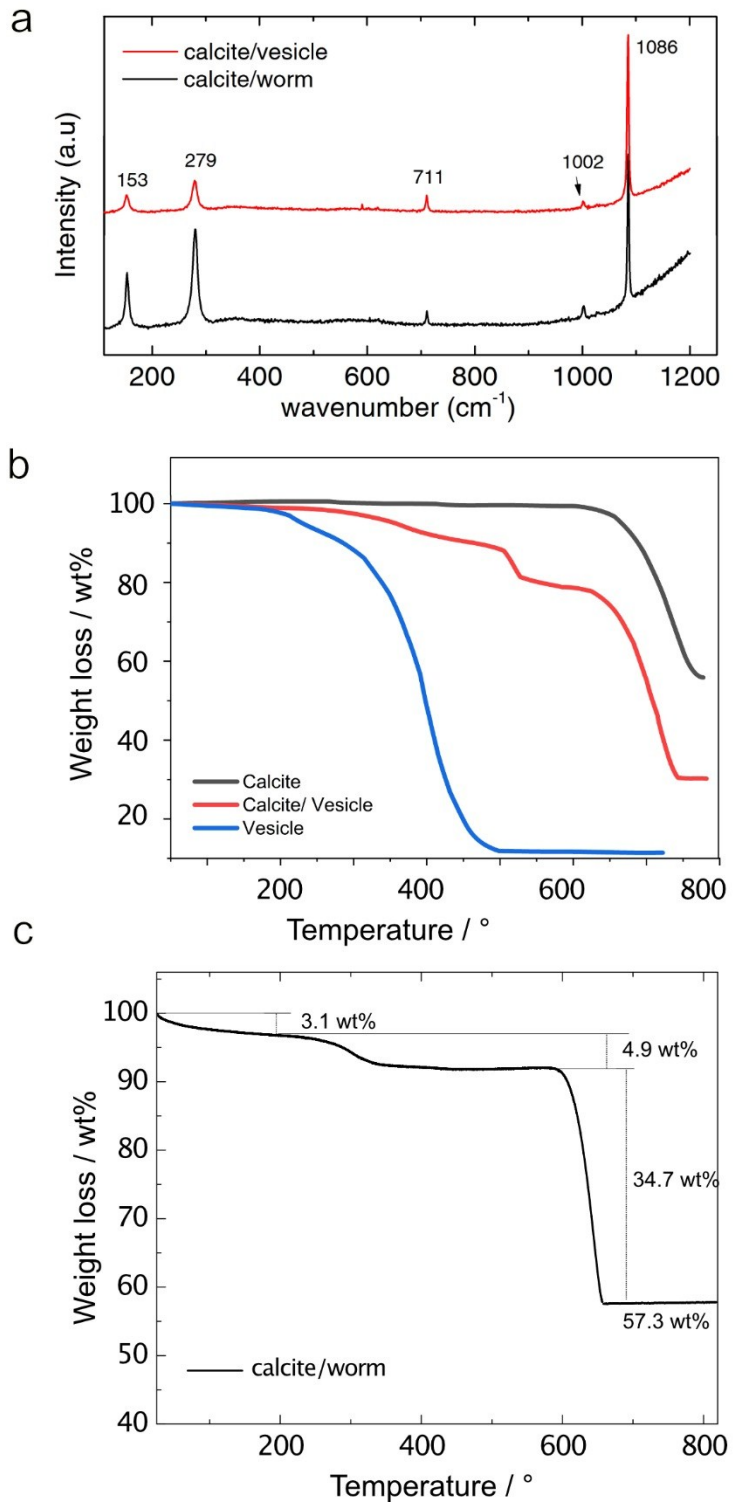

Figure S2: Raman Spectra and Thermogravimetric Analysis of Nanocomposites. (a) Raman spectra of calcium carbonate nanocomposite crystals. The $CaCO_3$ polymorphs can be identified based on characteristic peaks, where the v_1 (1085 cm^{-1}) and v_4 (711 cm^{-1}) peaks

correspond to the CO_3^{2-} symmetric stretch and symmetric bending respectively, and two lattice mode peaks at 281 and 155 cm^{-1} are also shown. The peak at 1002 cm^{-1} derives from the copolymers. (b) TGA profiles of vesicle/calcite nanocomposites, calcite and the pure vesicles collected in air, where these have been reported previously[2] and, (c) TGA of worm/calcite nanocomposites collected under nitrogen.[3]

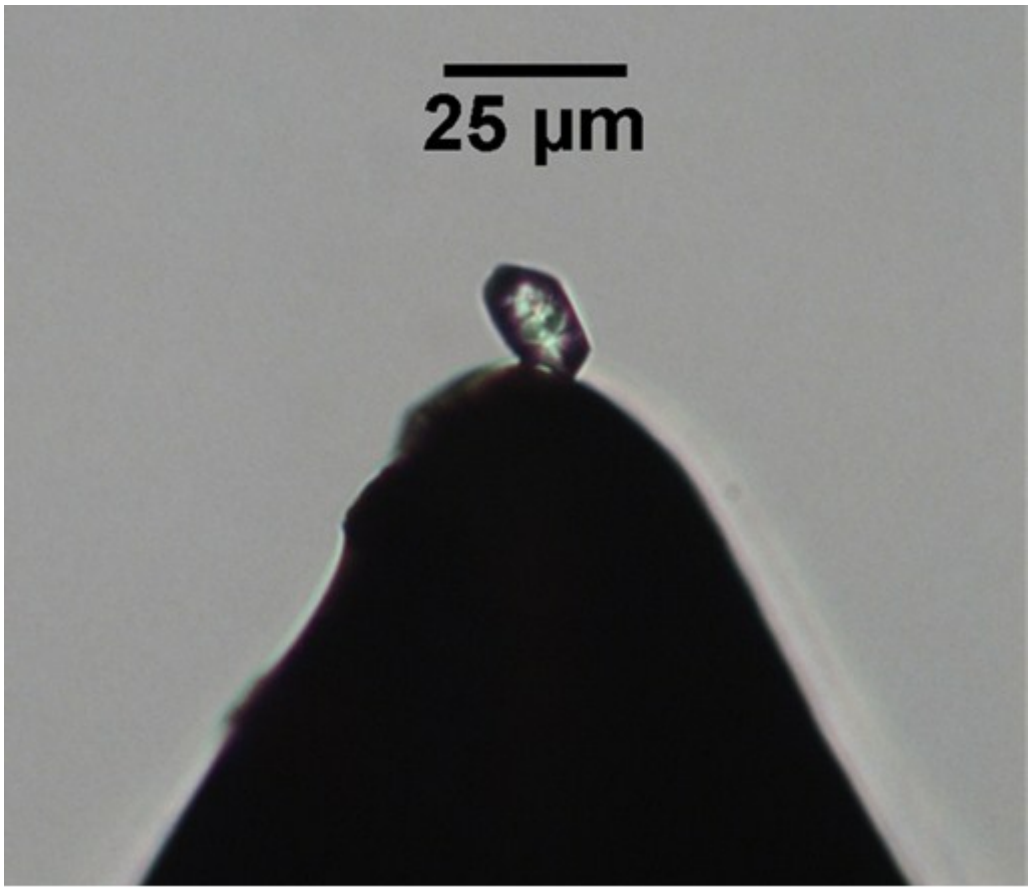

Figure S3: Optical Micrograph of a Single Crystal Mounted for Ptychographic X-ray Computed Tomography.

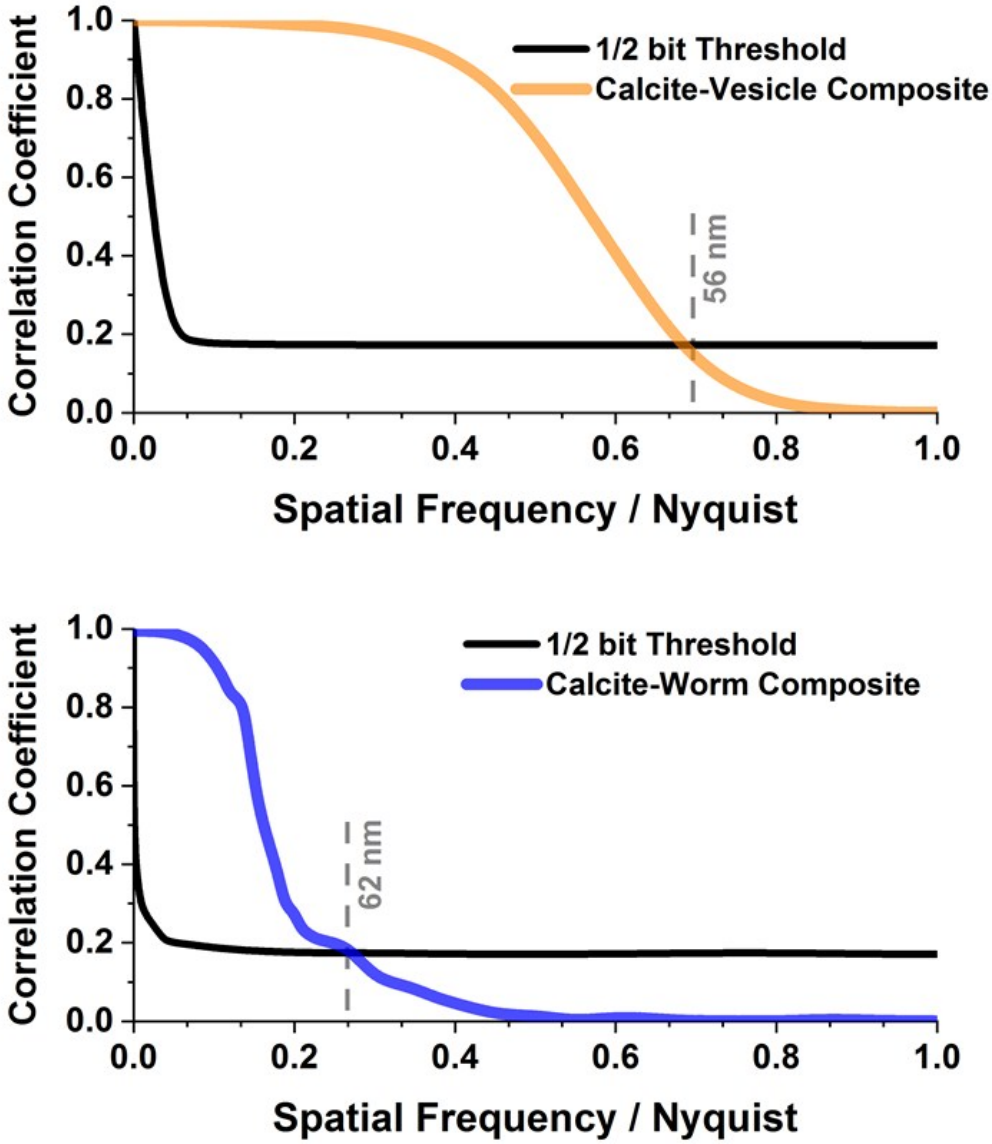

Figure S4. Spatial Resolution of Ptychographic Tomograms. Fourier shell correlation (FSC) line plots of the electron density tomograms. The selected threshold for determining the resolution is the ½ bit criterion.[22] Voxel sizes are $(38.82\ nm)^3$ for the calcite/vesicle crystal and $(16.66\ nm)^3$ for the calcite/worm crystal. The spatial resolution is estimated to be around 56 nm and 62 nm respectively.

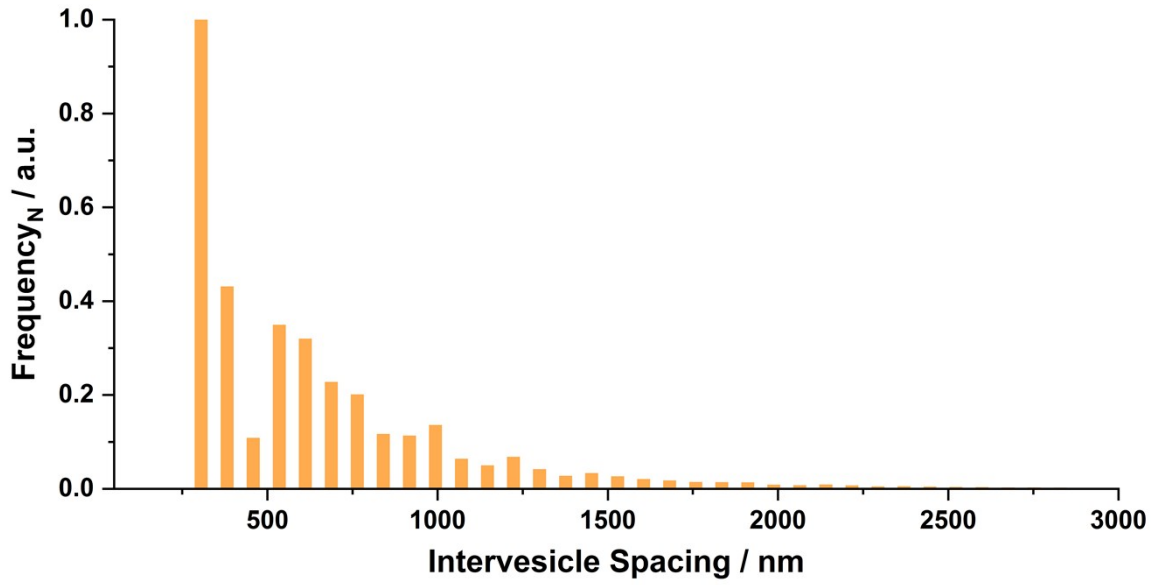

Figure S5: Distribution of Inter-vesicle Spacing in the Imaged Silica-Loaded Copolymer Vesicle Calcite Nanocomposite.

Supporting Movie 1: Volume Rendering of the Calcite/Vesicle Ptychographic Tomogram. Shown are the volume reconstruction of and cut slices through the retrieved electron density tomogram as well as the component-segmented tomogram. The beam direction is along the z axis, with the y axis vertical, while the sample holder is placed normal to the beam direction (z).

Supporting Movie 2: Volume Rendering of the Calcite/Worm Ptychographic Tomogram. Shown are the volume reconstruction of and cut slices through the retrieved electron density tomogram. The beam direction is along the z axis, with the y axis vertical, while the sample holder is placed normal to the beam direction (z).

References:

1. M. Semsarilar, E. R. Jones, A. Blanazs and S. P. Armes, *Advanced Materials*, 2012, **24**, 3378-3382.
2. Y. Ning, D. J. Whitaker, C. J. Mable, M. J. Derry, N. J. W. Penfold, A. N. Kulak, D. C. Green, F. C. Meldrum and S. P. Armes, *Chemical science*, 2018, **9**, 8396-8401.
3. Y. Y. Kim, M. Semsarilar, J. D. Carloni, K. R. Cho, A. N. Kulak, I. Polishchuk, C. T. Hendley, P. J. M. Smeets, L. A. Fielding, B. Pokroy, C. C. Tang, L. A. Estroff, S. P. Baker, S. P. Armes and F. C. Meldrum, *Advanced Functional Materials*, 2016, **26**, 1382-1392.
4. M. Dierolf, A. Menzel, P. Thibault, P. Schneider, C. M. Kewish, R. Wepf, O. Bunk and F. Pfeiffer, *Nature*, 2010, **467**, 436-439.
5. P. Thibault, M. Dierolf, A. Menzel, O. Bunk, C. David and F. Pfeiffer, *Science*, 2008, **321**, 379-382.
6. J. Ihli, A. Diaz, Y. Shu, M. Guizar-Sicairos, M. Holler, K. Wakonig, M. Odstrcil, T. Li, F. Krumeich, E. A. Müller Gubler, W.-C. Cheng, J. A. van Bokhoven and A. Menzel, *The Journal of Physical Chemistry C*, 2018, DOI: 10.1021/acs.jpcc.8b05624.
7. M. Holler, J. Raabe, R. Wepf, S. H. Shahmoradian, A. Diaz, B. Sarafimov, T. Lachat, H. Walther and M. Vitins, 2017, **88**, 113701.
8. M. Lebugle, M. Liebi, K. Wakonig, V. A. Guzenko, M. Holler, A. Menzel, M. Guizar-Sicairos, A. Diaz and C. David, *Opt. Express*, 2017, **25**, 21145-21158.
9. P. Kraft, A. Bergamaschi, C. Bronnimann, R. Dinapoli, E. F. Eikenberry, H. Graafsma, B. Henrich, I. Johnson, M. Kobas, A. Mozzanica, C. M. Schleputz and B. Schmitt, *IEEE Transactions on Nuclear Science*, 2009, **56**, 758-764.
10. I. Johnson, A. Bergamaschi, H. Billich, S. Cartier, R. Dinapoli, D. Greiffenberg, M. Guizar-Sicairos, B. Henrich, J. Jungmann, D. Mezza, A. Mozzanica, B. Schmitt, X. Shi and G. Tinti, *Journal of Instrumentation*, 2014, **9**, C05032.
11. M. Holler, A. Diaz, M. Guizar-Sicairos, P. Karvinen, E. Färm, E. Härkönen, M. Ritala, A. Menzel, J. Raabe and O. Bunk, *Scientific Reports*, 2014, **4**, 3857.
12. M. Holler and J. Raabe, *OPTICE*, 2015, **54**, 054101-054101.
13. X. Huang, H. Yan, R. Harder, Y. Hwu, I. K. Robinson and Y. S. Chu, *Opt. Express*, 2014, **22**, 12634-12644.
14. A. Kaestner, B. Münch, P. Trtik and L. Butler, *OPTICE*, 2011, **50**, 123201-123209.
15. M. Guizar-Sicairos, I. Johnson, A. Diaz, M. Holler, P. Karvinen, H.-C. Stadler, R. Dinapoli, O. Bunk and A. Menzel, *Opt. Express*, 2014, **22**, 14859-14870.
16. M. R. Howells, T. Beetz, H. N. Chapman, C. Cui, J. M. Holton, C. J. Jacobsen, J. Kirz, E. Lima, S. Marchesini, H. Miao, D. Sayre, D. A. Shapiro, J. C. H. Spence and D. Starodub, *Journal of Electron Spectroscopy and Related Phenomena*, 2009, **170**, 4-12.
17. M. Guizar-Sicairos and J. R. Fienup, *Opt. Express*, 2008, **16**, 7264-7278.
18. P. Thibault and M. Guizar-Sicairos, *New Journal of Physics*, 2012, **14**, 063004.
19. M. Guizar-Sicairos, A. Diaz, M. Holler, M. S. Lucas, A. Menzel, R. A. Wepf and O. Bunk, *Opt. Express*, 2011, **19**, 21345-21357.
20. M. Guizar-Sicairos, J. J. Boon, K. Mader, A. Diaz, A. Menzel and O. Bunk, *Optica*, 2015, **2**, 259-266.
21. A. Diaz, P. Trtik, M. Guizar-Sicairos, A. Menzel, P. Thibault and O. Bunk, *Physical Review B*, 2012, **85**, 020104.
22. M. van Heel and M. Schatz, *Journal of Structural Biology*, 2005, **151**, 250-262.
23. M. Semsarilar, V. Ladmiral, A. Blanazs and S. P. Armes, *Polymer Chemistry*, 2014, **5**, 3466-3475.

24. C. Gonzato, M. Semsarilar, E. R. Jones, F. Li, G. J. P. Krooshof, P. Wyman, O. O. Mykhaylyk, R. Tuinier and S. P. Armes, *Journal of the American Chemical Society*, 2014, **136**, 11100-11106.